IEEE Access
Multidisciplinary | Rapid Review | Open Access Journal

Received May 4, 2020, accepted June 1, 2020, date of publication June 11, 2020, date of current version June 24, 2020.

Digital Object Identifier 10.1109/ACCESS.2020.3001578

An Efficient Region Precise Thresholding and Direct Hough Transform in Femur and Femoral Neck Segmentation Using Pelvis CT

YOUNG-JI YUN[1], (Graduate Student Member, IEEE), BYEONG-CHEOL AHN[2,3], MUTHU SUBASH KAVITHA[4], AND SUNG-IL CHIEN[1], (Member, IEEE)

[1]School of Electronics Engineering, Kyungpook National University, Daegu 41566, South Korea
[2]Department of Nuclear Medicine, School of Medicine, Kyungpook National University, Daegu 41944, South Korea
[3]Department of Nuclear Medicine, Kyungpook National University Hospital, Daegu 41944, South Korea
[4]Graduate School of Advanced Science and Engineering, Hiroshima University, Higashihiroshima 739-8511, Japan

Corresponding authors: Muthu Subash Kavitha (kavitha@hiroshima-u.ac.jp) and Sung-Il Chien (sichien@ee.knu.ac.kr)

This work was supported by the BK21 Plus Project funded by the Ministry of Education, South Korea, under Grant 21A20131600011 and MSK thanks Japan Society for the Promotion of Science (JSPS) KAKENHI under Grant 18F18112.

ABSTRACT This study proposed a fully-automated method for the segmentation of the femur and femoral neck in volumetric computed tomography (CT) images for the evaluation of osteoporotic fractures with severe abnormalities. We evaluated the proposed method on pelvis CT image of 30 patients for both the left and right sides. The proposed framework consists of three components: (1) localization of the acetabulum from the femoral head by tracing the intensity and adjacent neighbors of bone pixels, (2) segmentation and enhancement of the femur from its surrounding tissue using multi-level thresholding with filtering techniques, and (3) extraction of femoral neck contours using a directed Hough transform with oriented contour-filling techniques. The quality of the proposed femur segmentation performance was compared with the segmentation results using an edge-based active contour model (ACM), active shape model (ASM) and ground truth including average precision, recall, false-positive rate (*FPR*), false-negative rate (*FNR*), and the Dice similarity coefficient (*DSC*). The proposed method showed error of less than 1% for femur segmentation. A highly satisfactory similarity agreement was achieved between automated and manual methods, with a *DSC* greater than 94.8—exceeding those of semi-automated segmentations of the femur. Quantitative and qualitative experimental results indicated that the proposed fully-automated approach was capable of accurately segmenting the femur and femoral neck, which suggests the possibility of reducing insignificant contours of bone structures for further assessment of risk for osteoporotic fractures.

INDEX TERMS Acetabulum, bone segmentation, computed tomography, femoral neck, femur.

I. INTRODUCTION

Osteoporosis is characterized by deterioration of bone tissue and associated with an increased risk of morbidity and mortality [1]. Hip fractures have the most serious issues, needed hospitalization and major surgery. Early analysis of osteoporosis is important to prevent osteoporotic fracture. Bone mineral density (BMD) assessment via dual-energy x-ray absorptiometry is a commonly available tool to measure the bone strength. Intracapsular fractures of the femoral neck significantly affect both the cortical and trabecular bone [2]. Hence, precise femur and femoral neck region segmentation on volumetric computed tomographic images (CT) is useful in recognizing BMD and geometric features for surgical planning and postoperative assessment [3]. However, the segmentation of a femur from a CT volume presents several difficulties: i) partial volume effect, ii) varying bone size and shape between individuals, and iii) dispersed and weak edges of bone. To overcome these problems, manual and semi-automated femur or femoral neck detection systems have been developed [4]–[6]. However, the segmentation accuracy of these techniques is highly reliant on expert individuals and also time-consuming. Therefore, a fast and robust segmentation of femur and femoral neck for geometrical

The associate editor coordinating the review of this manuscript and approving it for publication was Carmelo Militello.

features, without user intervention, would be useful to assess the risk of osteoporotic fracture in individuals with severe abnormalities.

Most research studies are focused on thresholding-based techniques [7]–[10] for bone segmentation since the higher intensity values of bone are more informative for the separation of bone from the surrounding soft tissue on CT images [11], [12]. However, local thresholding approaches are influenced by intensity in homogeneities [8], [9] and produce poor segmentation results in detecting low-contrast bone contours.

Most recently, some popular model based segmentation methods were proposed such as the statistical shape model and Atlas based segmentation [13]–[19]. The statistical shape models are used for femur segmentation. The kinds of typical models are active contour model (ACM), active shape model (ASM), active appearance model (AAM) [13]–[17]. These models initialized contour points through the training process or manually segmentation. And contour points are deformed into the shape of target. The object detection and segmentation that use shape- and appearance-based models require positioning landmarks on the contour of bones on the training images [20], [21]. However, the shape of the femur is different for each person and requires generating many templates of the high-variability of the femoral contour to produce large datasets. Although shape-based techniques are simple, manual positioning is tedious and time-consuming. The Atlas based segmentation is used for segmentation of anatomical image structure and bone [18], [19]. This method registers the labeled image which is also called the Atlas image. Those models detect the part of the target image which is most similar with the labeled image. For segmenting an object, both the statistical shape models and Atlas based segmentation need the information of the shape and orientation for alignment of the trained and target objects.

A deep learning segmentation network is used to perform pixel-wise classification of femoral analysis [22], [23]. However, deep learning frameworks require abundant training and ground truth data. Furthermore, the aforementioned methods of the femur detection do not address the segmentation performance of unevenly-distributed bone tissue with holes between the femoral head and hip joint space. This is considered a severe abnormality group and the most complex for segmentation, according to [9], [24]. Hence, this study addresses the segmentation of femur and femoral neck in severely-diseased hip joints based on the distribution of regional characteristics. The extraction of the femoral neck is highly dependent on the position of the evenly-distributed femoral head. Hence, the extraction of the femoral neck from a severely abnormal or unevenly-distributed femur without manual intervention is one of the most important prerequisites of osteoporotic fracture identification.

In this study, we proposed a fully-automated framework for the segmentation of the acetabulum, femur, and femoral neck on both the left and right sides of a hip joint CT with severe abnormalities using region-precise intensity distributions, adjacent neighbor pixels, and Hough transform techniques as shown in Fig. 1. The performance of the proposed automatic segmentation results was compared with the semi-automatic segmentations of the femur by using an ACM and ASM. Various performance metrics were used to evaluate the potential benefit of our proposed automatic technique based on the manual segmentation of the femur.

II. MATRIALS AND METHODS

To evaluate our proposed automatic method, we used coronal pelvis CT scans of 30 subjects which included 13 males and 17 females between 30 and 90 years old, who had also undergone BMD evaluation. The Institutional Review Board of Kyungpook National University Hospital approved the study protocol. Images were acquired by means of a CT scanner (GE Medical Systems, Madison, WI) with a voxel size of 1 mm and a slice interval of 1.5 mm. The number of CT image slices for each patient ranged from 50 to 90. Based on the T-score value of femoral BMD, out of 30 subject's, 13 did not have osteoporosis, 13 were osteopenia, and 4 were determined to have osteoporosis. BMD evaluation was performed on the femoral neck with the use of dual-energy x-ray absorptiometry (GE Healthcare, Madison, WI). The subjects were classified as normal (T-score ≥ -1.0), osteopenia (T-score between -1 and -2.5), or osteoporotic (T-score ≤ -2.5) at each skeletal site according to the World Health Organization guidelines. The ground truth segmentation of the proximal femur was generated by manual selection of the femoral contour on CT images through Adobe Photoshop CS5 that allows generating two regions defined as proximal femur and the background. The coronal slices correspond to the image sizes from the beginning to the ending of the femoral neck were used for generating the ground truth masks.

A. AUTOMATED SEGMENTATION OF THE FEMUR AND FEMORAL NECK

The proposed region-based segmentation framework for femur and femoral neck with severe abnormalities is illustrated schematically in Fig. 1. The proposed framework consists of three parts: i) segmentation of the acetabulum from the femoral head, ii) segmentation and enhancement of the femur from its surrounding tissue, and iii) extraction of the femoral neck. The number of slices above and below the center slice that portray the shape of the femoral head and bone were included for volumetric detection of the femur and femoral neck. In pelvis CT, we initially selected the femoral slices which correspond to the images from the beginning to the ending of the femoral neck. Most of the image sizes are fixed to be 512×512 pixels except three images of which the sizes are 512×523, 512×527, and 658×527. In addition, we also chose the center slice which has the largest and most prominent part of the femur. Thereafter, we proceed to the segmentation of the femoral neck using the center slice. The size of the femur is almost similar from patient to patient and its position is also located nearly in the similar place because the original size of the image is fixed. The

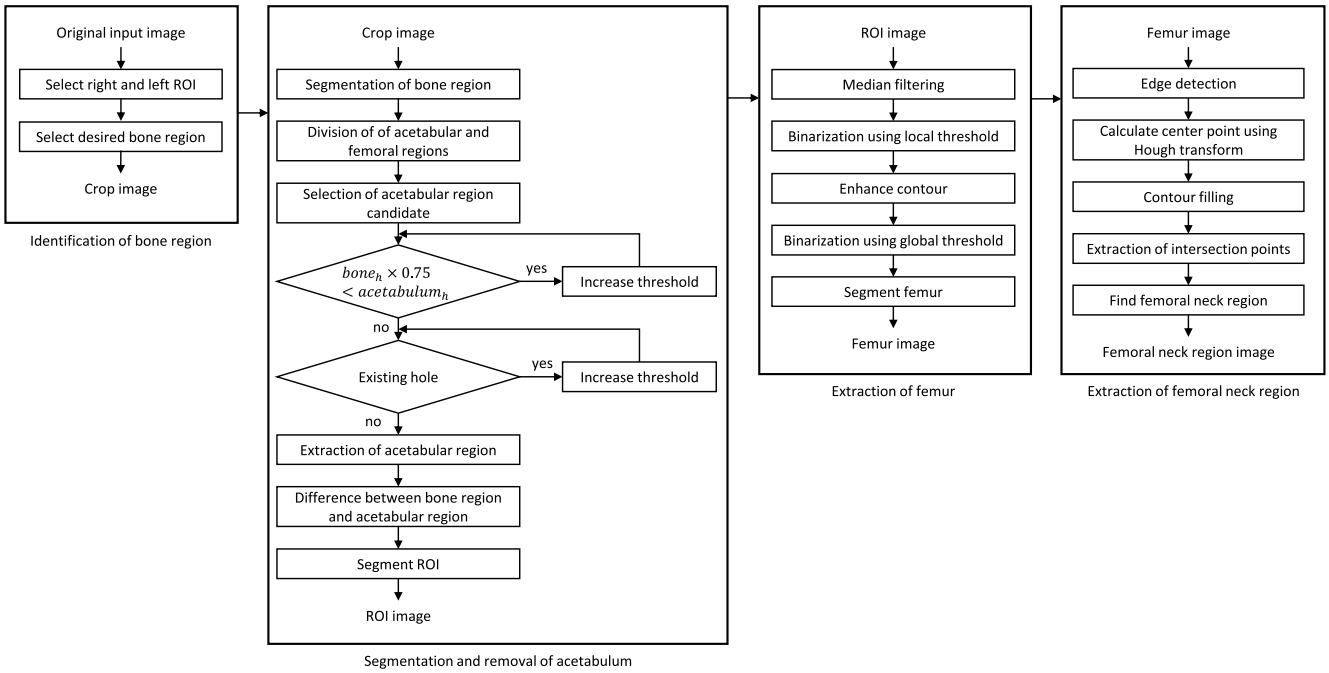

FIGURE 1. Proposed region-based segmentation framework for femur and femoral neck with severe bone abnormalities.

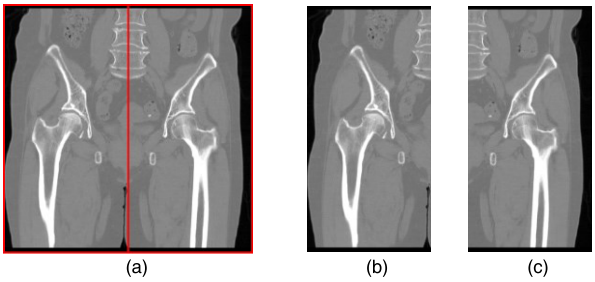

FIGURE 2. Selection of both right and left ROI from coronal pelvis CT for the segmentation framework: (a) original image, (b) right hip, and (c) left hip.

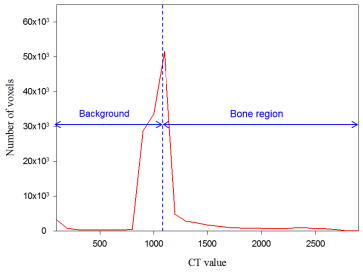

FIGURE 3. Location of distribution of bone region using histogram-based thresholding.

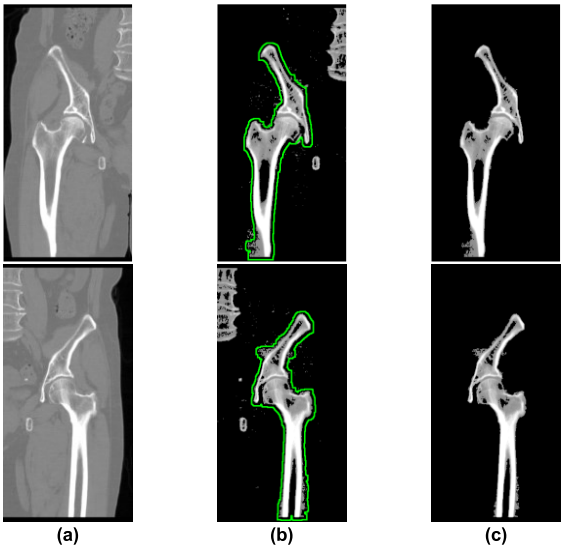

FIGURE 4. Selection of desired right (upper row) and left (lower row) bone regions for segmentation: (a) input image, (b) thresholding image, and (c) labeling image using centroid and area size.

original image width was considered when selecting both the left and right hip region of interest (ROI) by calculating a window size of (half of width × height) pixels for each image, as shown in Fig. 2. Both the left and right hip ROI were subjected to the segmentation framework. First, we applied a thresholding technique to locate the distribution of the bone region. The value was initialized to an intensity of 900, which is defined as the starting threshold based on the histogram. It was increased incrementally by an intensity of 100 until a single object of bone region was located. The first bone region was located at an intensity of 1100 as shown in Fig. 3. The connected component labeling was used to preserve the largest connected component object of desired bone region while removing unwanted objects (Fig. 4).

B. SEGMENTATION OF ACETABULUM

In this part of our study, we focused on the detection of the acetabulum for a femoral contour, which was one of

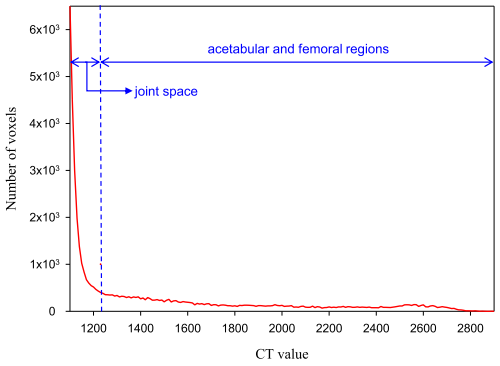

FIGURE 5. Histogram-based thresholding for the separation of acetabulum from femoral region.

FIGURE 6. Tracing of acetabulum on both right and left ROI: (a) thresholding image and (b) labeling image using centroid trace of acetabulum (red contour) and femur (green contour).

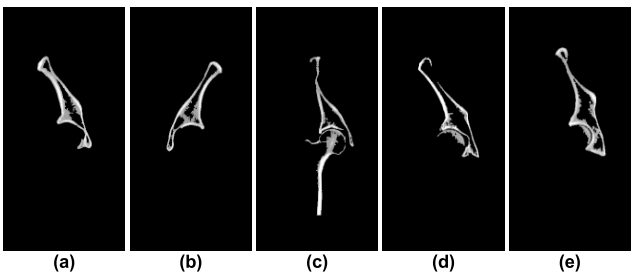

FIGURE 7. Extraction of acetabular region candidates: (a)(b) accurate segmentation results and (c)(d)(e) failure segmentation results.

our most challenging tasks. The evenly distributed bone contour region showed relatively higher intensity than both the area inside the bone regions and the area between the acetabulum and femoral head. To find two objects of bone regions, we further increased the thresholding value, and the results vary for each image depending on its precise region as shown in Fig. 5. The labeling technique was used to

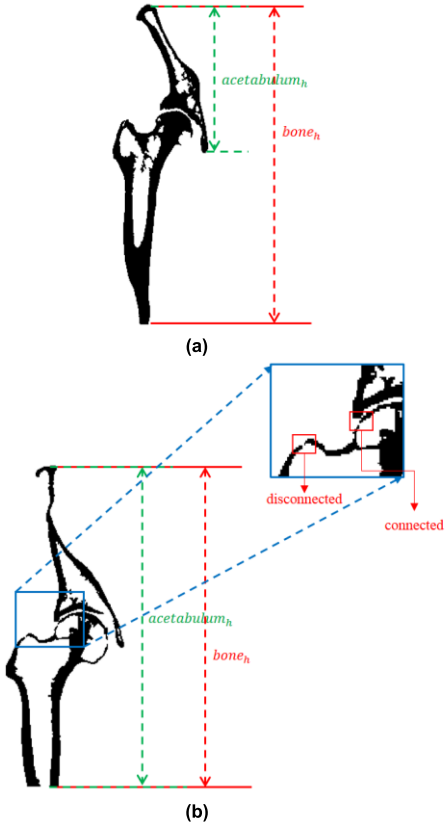

FIGURE 8. Extraction of acetabular region candidate using height: (a) $acetabulum_h$ is shorter than a certain ratio $bone_h$ and (b) $acetabulum_h$ is same length as $bone_h$.

obtain the centroid of each bone region; the upper acetabulum is represented by the red contour, and the lower femur is represented by the green contour (Fig. 6). Examples of successful segmentation of the acetabulum are presented in Figs. 7(a) and 7(b). However, the task of segmenting the acetabulum failed in cases where the femoral head was close to the upper region (Figs. 7(c), 7(d), and 7(e)). This procedure was not effective for unevenly distributed bone tissue in a severely narrowed inter-bone region. Therefore, due to the asymmetry of the human body, severely affected bone exhibited over-segmentation of the acetabulum. Furthermore, the gap between the acetabulum and the femoral head varies with different images [25]. The over-segmentation results were corrected using two methods based on the total height of the bone and the size of the joint space, as follows:

1) Measurement of bone height: The total height of all the bones and the height of the acetabulum were used to segment the acetabulum (Fig. 8). From the previous procedure, we have two segmented regions. Usually, the normal situation is that the upper region is the acetabulum, and the lower region is the femur. The height of the upper region is regarded as that of the acetabulum. Still, there is a special case that the acetabulum is connected to the femoral head and the small fragment of the femur is recorded as an independent region. Hence, height of such a large region is wrongly

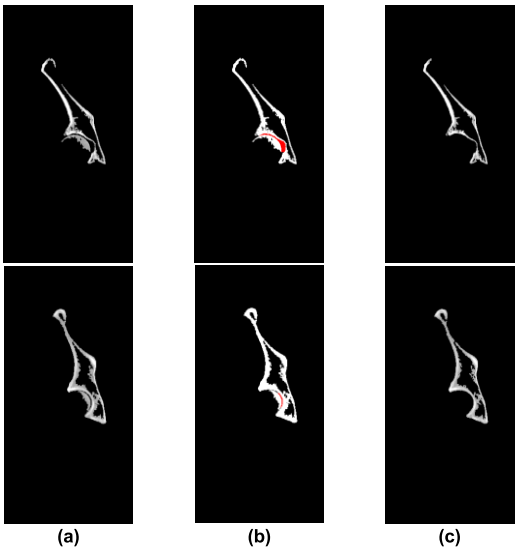

FIGURE 9. Removal of joint space from acetabulum: (a) joint space image, (b) labeling image, and (c) removal of joint space image.

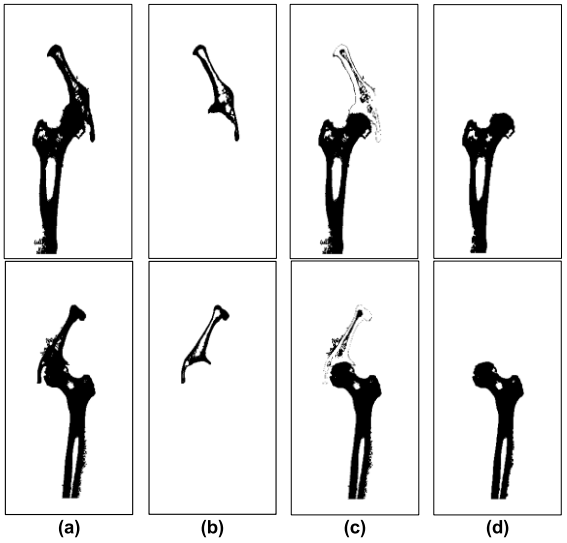

FIGURE 10. Segmentation of femoral region candidate: (a) whole bone region, (b) acetabulum, (c) subtraction of acetabular image of (a) from (b), and (d) resultant femur.

calculated as that of the acetabulum. If the height of the acetabulum is almost equal to the height of all the bones, the method of increasing our prior threshold intensity incrementally by 10 can separate the acetabulum from the femoral head region. At every incremented step we check whether the following condition is satisfied:

$$bone_h \times 0.75 > acetabulum_h, \tag{1}$$

where $bone_h$ and $acetabulum_h$ are height of all the bones and height of acetabulum. This process extracts the acetabulum from touching the femoral head.

2) Measurement of joint space size: The segmented acetabulum in some cases was still attached to the surface of the femoral head (Fig. 9(a)). To remove the joint space, we first applied the distance transform method twice to trace the acetabular pixels from left to right and then from top to bottom to extract the object pixels surrounded by high-intensity bone region [26], [27]. Second, we multiplied and applied region labeling to the two resultant traced images of acetabular pixels from left to right and then from top to bottom, which calculated the area of the joint space pixels [28]. An area greater than 100 pixels was detected as the joint space region (Fig. 9(b)). Finally, the detected joint space between the acetabulum and femur was removed by applying the thresholding-based technique of incrementally increasing the intensity by 10 beyond the prior threshold until the joint space was removed (Fig. 9(c)). These procedures were automatically performed for all over-segmented slices.

C. SEGMENTATION AND ENHANCEMENT OF FEMUR

In this part of our study, we aimed to trace and enhance the contour of the femur. We obtained the femur by subtracting the segmented acetabulum in Fig. 10(b) from Fig. 10(a). Then, we extracted the region with the largest area from the whole bone region by using connected component labeling. However, the extracted femoral contour exhibited artifacts; accordingly, the enhancement of bone contour is essential to the extraction of the femoral neck [29]–[31]. To segment the femoral neck more precisely, we converted all of the voxels between 0 and 255 intensity. Then, we used 3×3 median filtering to reduce the noise surrounding the femoral region. The resulting image was converted into a binary image. Binarization with simple thresholding is not suitable because it removes important information from the weak contour. Therefore, we used two-step binarization. In the first step, we used a contour mask of 5×5 pixels to calculate the threshold [29]. In the second step, we implemented an Otsu's thresholding technique for the selection of an automatic threshold. Finally, we multiplied the maximum size of the region mask by 1.5 intensity to enhance the femoral region. Fig. 11 shows the segmentation and enhancement results after using the techniques described in this section.

D. EXTRACTION OF THE FEMORAL NECK REGION

Identification of the femoral head contour is essential for the subsequent process of identifying the neck region. However, the automatic estimation of the femoral neck in a severely affected bone CT image was another challenging task in this study. To extract the femoral neck, we performed the following steps:

1) We applied Canny edge detection to determine the contours of the bone object (Fig. 12(b)).
2) The circle detection Hough transform method was used to determine the center point of the femoral head [32]; the radius was not used to calculate the circle. The directed Hough transform algorithm is described by five steps:

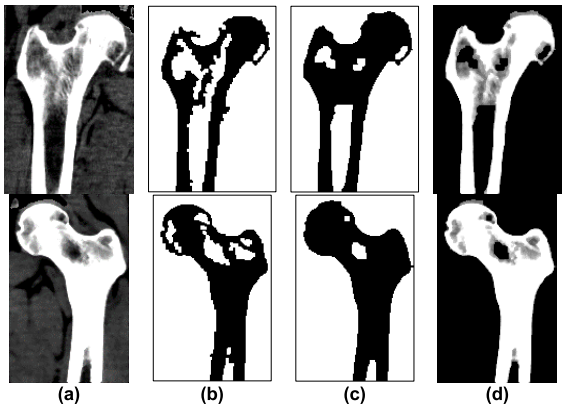

FIGURE 11. Enhancement of femur: (a) original femur image, (b) local thresholding using 5 × 5 mask, (c) Otsu's thresholding image, and (d) femoral region.

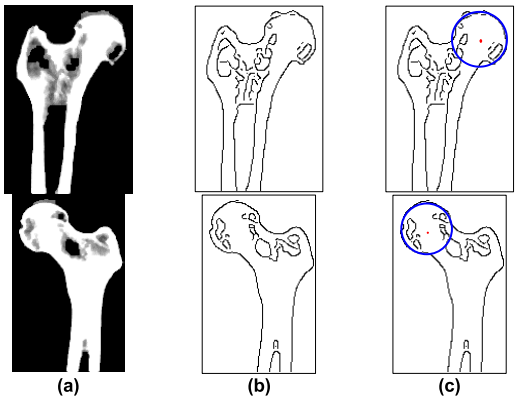

FIGURE 12. Center point detection using Hough transform: (a) femoral region, (b) Canny edge, and (c) center point using Hough transform.

i) Quantize the parameter space for parameters a and b of a circle.
i) Initialize the accumulator array $M(a, b)$ to zero.
ii) Compute the gradient magnitude $G(x, y)$ and angle $\theta(x, y)$.
iii) For each edge point in $G(x, y)$, increment all points in the accumulator array $M(a, b)$ along a line using the following equation:

$$b = atan\theta - xtan\theta + y \tag{2}$$

iv) Determine the center point of the femoral head using the local maxima in the accumulator array, shown as a red point in Fig. 12(c).

The starting point of the femoral neck position was measured from the center point along the smallest distance tangent lines. However, the disconnected femoral head contour strongly influenced the measurement of the neck position, as shown in Fig. 13(a).

3) To fill the contour discontinuities, an automatic contour filling technique based on various orientations was used 33]. It extracted r candidate points on the femoral head from the center point using orientation angles from −45° to 180°. Contour discontinuities were identified where the average of the r candidate points was higher than the average value of $r \times 0.75$ by an experiment. In Fig. 13(b), red points represent r candidate points,green points represent the disconnected contour, and blue points represent filling the contour.

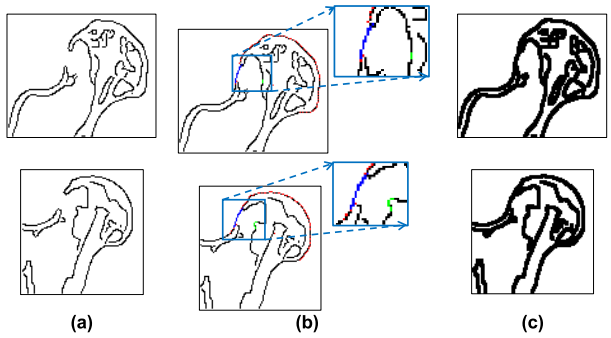

FIGURE 13. Filling femoral head contour: (a) Canny edge, (b) contour filling, and (c) morphological dilation.

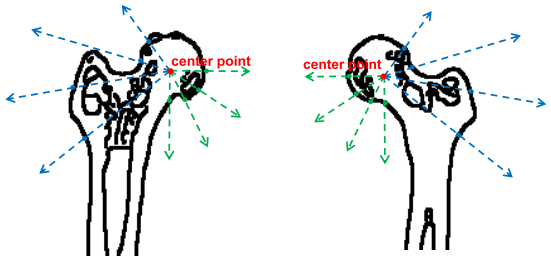

FIGURE 14. Tracing starting point from center point for femoral neck.

4) Finally, morphological dilation was applied after the contour filling, as shown in Fig. 13(c).
5) Measurement of the starting point position for femoral neck detection was achievable after the missing contour was filled. It was achieved by calculating the minimum distance from the center point to the neck points of both the right and left side of the femoral head, as shown in Fig. 14. The neck candidate point positions were detected at every 2 to 3 intervals, which represents the minimum distance. The estimated points were connected to form a straight line as shown in Fig. 15(b). The femoral head left side was more curved than the right side; accordingly, the ending point was traced from the left side with from 0° to 3° slope relative to the starting point. Similarly, the ending point for the right side was detected by fixing the same value for the left side starting-to-ending-point distances. Finally, the entire contour was connected through the estimated points, segmenting the femoral neck region as shown in Fig. 15(c).
6) Similarly, the starting and ending points of the neck region and slope were measured on both right and left sides of all femoral slices to extract the femoral neck region to enable the estimation of osteoporotic fracture risk (Fig. 16).

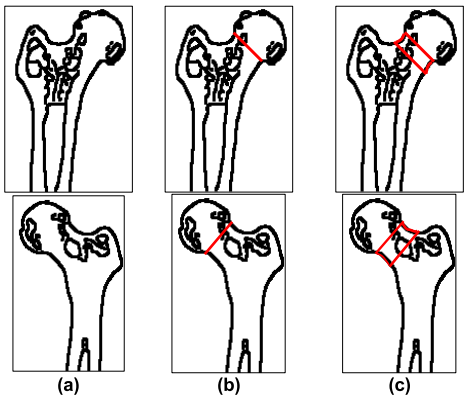

FIGURE 15. Extraction of femoral neck: (a) Canny edge, (b) upper contour of femoral neck, and (c) femoral neck contour.

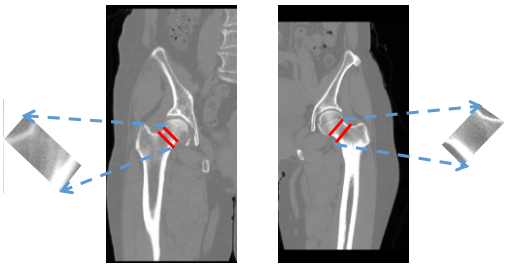

FIGURE 16. Femoral neck extraction results of hip ROI.

III. MODELS BASED ON ACTIVE CONTOUR AND ACTIVE SHAPE FOR FEMUR SEGMENTATION

We adopted an edge-based active contour model (ACM) to detect the femoral contour in this study [34]. The traditional ACM or snake has been widely applied in image analysis applications for the segmentation of desired objects, but it is weak in detecting sudden changes in the perimeter of an object [34], [35]. It is a list of ordered points: a continuous parametric function $(\mathbf{x}(s), \mathbf{y}(s))$, where the ranges of s are [0, 1] and defined as:

$$E^*_{snake} = \int_0^1 (E_{internal}(\mathbf{v}(s)) + E_{external}(\mathbf{v}(s)) + E_{image}(\mathbf{v}(s)))ds. \quad (3)$$

$$\mathbf{v}(s) = (\mathbf{x}(s), \mathbf{y}(s)), \quad (4)$$

where $E_{internal}$, $E_{external}$, and E_{image} are internal energy, external energy, and image energy. The edge-based ACM used in this study was calculated using the location of the contour on the plane to evaluate its energy value. In subsequent iterations, the contour balanced its location to the desired object in the image, which modified its shape to minimize its energy. The developed mask image using the set of selected initial points was used to cover the input image. The number of iterations was optimized to 100, which reduced the contour to preserve foreground pixels from background pixel objects. Furthermore, we used active shape model (ASM) to segment the femur [36]. The landmark points were manually selected with twelve major points to cover the contour of the input image. The number of iterations was fixed to 100 and train the data set using three fold cross validation [37]. ASM worked well with regular and stable femoral shape and failed to detect the irregular bone contour shape was observed. The performance of the ACM and ASM methods in segmenting femur was compared with the proposed method and ground truth is shown in Fig. 17.

IV. EXPERIMENTAL SETUP AND EVALUATION

The proposed method was evaluated on 30 hip volumetric CT images. We evaluated the performance of the proposed method in segmenting femoral region with manual segmentation detected by an expert. Furthermore, we compared the proposed method with the ACM for the segmentation of femur. The performance evaluation was calculated by using performance metrics based on precision, recall, false-positive rate (*FPR*), false-negative rate (*FNR*), and the Dice similarity coefficient (*DSC*). Precision describes the ratio of correctly segmented locations to the total segmented locations, defined as $TP/(TP + FP)$. Recall demonstrates the ratio of correctly segmented locations to all observations in the actual class and is defined as $TP/(TP + FN)$. *FPR* and *FNR* are used to indicate misclassification error rates, defined as $FP/(FP + TN)$ and $FN/(FN + TP)$. The differences between proposed method and manual detection were evaluated in terms of *DSC*, which is defined as $DSC = 2(S \cap G)/(S + G)$, where S is the segmented femur by automatic method and G is the manually-detected femoral region. A *DSC* value of 0 denotes no similarity between the two segmented bone regions, and 1 indicates exact similarity. The segmentation framework developed in this study was implemented using Matlab 2018b (The Mathworks, Inc. Natick, MA, USA).

V. RESULTS

The qualitative performance of the proposed method in segmenting femoral regions was compared with the performance of the ground truth and ACM methods, as shown in Fig. 17. The qualitative results of the femoral contour were similar to the femoral contour of the ground truth. Due to the narrowed inter-bone regions, the competitive ACM method showed femoral contour discontinuity, which is not appropriate for fully-automated extraction of the femoral neck region. However, our proposed method accurately identified the femoral contour in weak and narrowed inter-bone regions. The proposed automatic approach resulted in a higher average precision (95.5%) and recall (99.2%) than with the semi-automatic ACM method, indicating the robustness of the proposed method in detecting the femoral contour for subsequent tasks (Table 1). The proposed method for segmenting femoral regions achieved low *FPR* and *FNR*, whereas the semi-automatic segmentation method produced high *FPR* and *FNR*. The *DSC* performance metric was 3.3% and 15.2% higher than with the ACM and ASM, respectively. The femoral contour detected by our proposed method is similar to ground truth. As a result, the proposed system can be used as a reliable system for accurate femoral neck extraction.

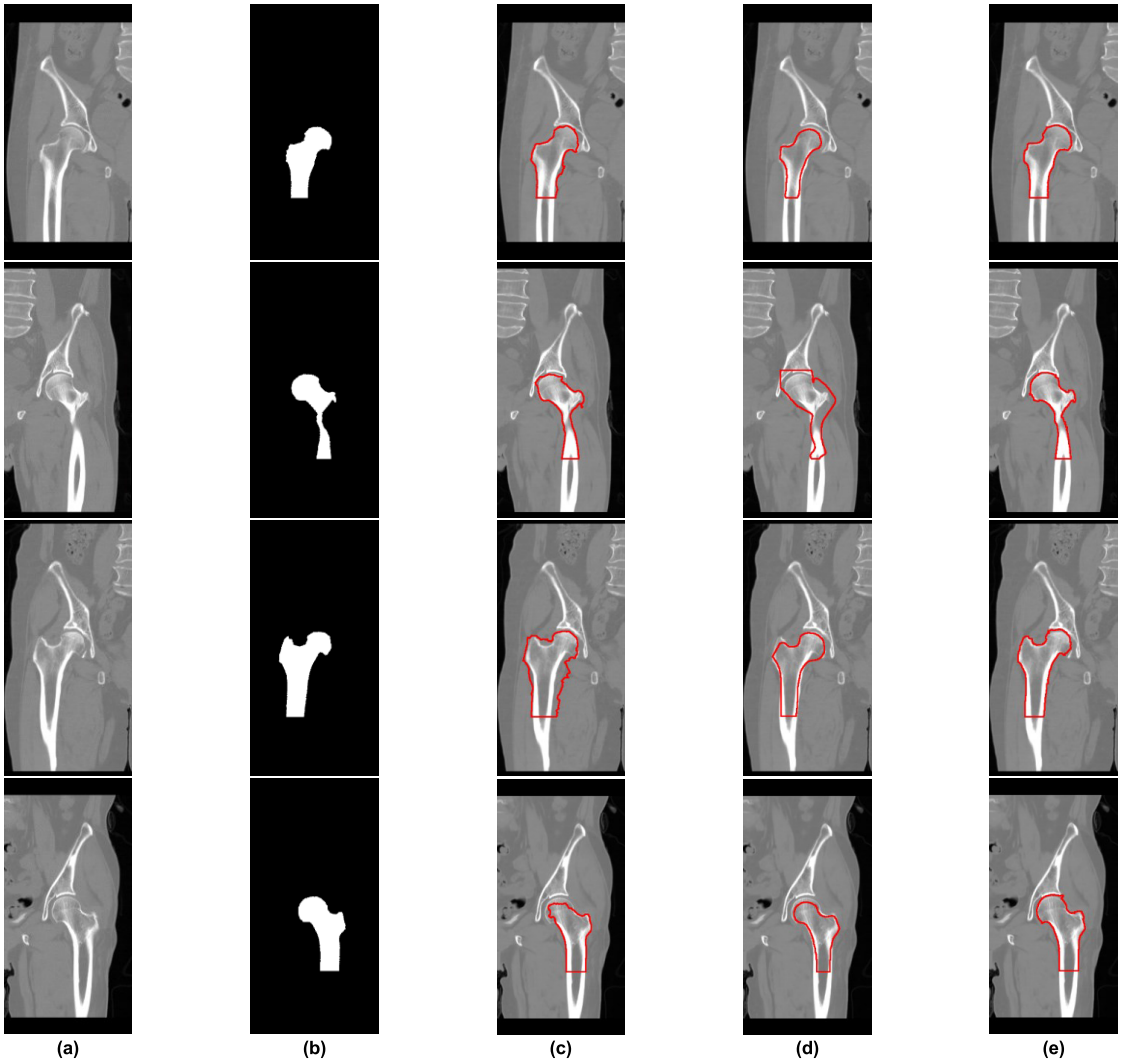

FIGURE 17. Segmentation results of femur on both right and left sides of the hip ROI: (a) input image, (b) ground truth image, (c) segmentation result of ACM, (d) segmentation result of ASM, and (e) segmentation result of proposed method.

TABLE 1. Comparison of performance proposed method with active contour and active shape models for femur segmentation.

Methods	Precision (%)	Recall (%)	*DSC* (%)	*FPR* (%)	*FNR* (%)
Proposed	95.5	99.2	94.8	0.003	0.81
ACM	85.4	98.9	91.5	0.01	1.07
ASM	89.9	73.7	79.6	0.56	26.31

TABLE 2. Comparison of execution time of propose method with active contour and active shape models for femur segmentation.

Methods	Execution time (sec)
Proposed	0.38
ACM	0.81
ASM	12.80

Next, we compare the execution time of the ACM and ASM measured the elapse times for 30 patients and averaged them. For the proposed method, we start to measure the elapse time when the center slice is located and continue until the femur is segmented. For the ACM and ASM, we start to measure the elapse time when the iterative procedure starts and continue until the femur is segmented. The result is shown in Table. 2. The proposed method, ACM, and ASM require 0.38, 0.81, and 12.8 sec on average, respectively to segment femur. The proposed method is about 2 and 33 times faster than the ACM and ASM, respectively. The ACM and ASM need enough iterative time to find the correct contour.

We also show the 3D visualization of surface rendering of the extracted femoral neck region from two perspective angles as shown in Fig. 18. The images of the first column are observed from the side and the images of the second column are approximately seen from up to bottom. For 3D visualization, we generate the femoral mask from the center slice and we apply it to all other slices. Thereafter, we use the 3D volume rendering software called RadiAnt DICOM

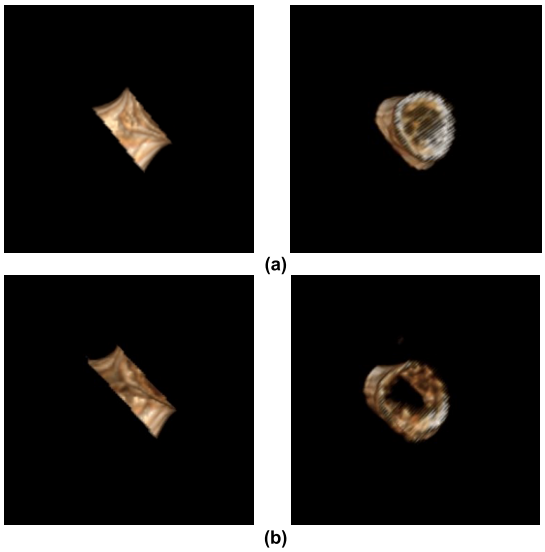

FIGURE 18. 3D visualization by surface rendering of extracted femoral neck region: (a) two perspective views of normal case and (b) two perspective views of osteoporotic case.

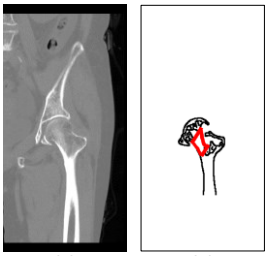

FIGURE 19. Failed example of proposed method: (a) input image and (b) result of edge detection and contour of femoral neck.

Viewer 5.5.1. Figs. 18(a) and 18(b) represent the normal and the osteoporotic case, respectively. The osteoporotic case has a hole inside the bone, because the osteoporotic patient shows low density in the inside bone called the trabecular bone. We infer that the osteoporotic patient has the trabecular bone of low density, leading to the hole of Fig. 18(b).

Next, we show the failed case caused by the proposed method as shown in Fig. 19. Fig. 19(a) is the input image and an example of osteopenia. As the bone density has decreased, the cortical bone becomes thinner. The contour of the femoral head and neck is not clear and the edge corresponding to the right part of the femoral head and neck is missing and the detected neck is different from the real one. The detected neck part is printed in red in Fig. 19(b). As a result, the starting points of the femoral neck are not detected correctly.

VI. DISCUSSION

To the best of our knowledge, most previous automatic analysis methods of proximal femur and femoral neck worked well in evenly distributed healthy bone but failed in unevenly distributed diseased bone and with noisy data [7]–[13]. This study proposed a fully-automated approach for the segmentation of femur and femoral neck in hip joint CT images, especially with severe abnormalities indicating a risk of osteoporotic fractures. The accurate segmentation of the femoral contour is important for the detection of the femoral neck; this study revealed that this automatic method for femoral region segmentation from CT images accurately matches the results achieved manually by an expert. The accuracy of the segmentation of the femur by our automatic method was quantitatively compared with the semi-automatic segmentation results by using an ACM and ASM. A highly satisfactory similarity agreement between automatic and manual methods ($DSC > 94.8$) was achieved that exceeded the semi-automatic method of femur segmentation. In addition, the average values of precision and recall evaluated for the segmentation of the femur using our approach were always greater than the semi-automatic ACM and ASM values for femoral contour detection.

This study achieved high segmentation performance for evenly distributed femur and enabled the consideration of hip joint space for unevenly-distributed bone tissue. The main contribution of this study was to demonstrate a method of separating the closely-overlapped joint space of the acetabulum and femoral head before segmentation. For this purpose, we developed a simple and effective intensity-based tracing technique without any user interaction that automatically enhances acetabulum and femur segmentation.

Although current automated methods produce accurate femur segmentation on healthy pelvic bone CT data, they yield unacceptable segmentation of the bone that poses variations in shape and blurred edges [6], [7]. The snake-based method using manual initialization wrongly detects the non-bone region as a bone structure and fails to detect the separation between bones [6]. Femur segmentation using computerized schemes on various orientations of bone skeletal structures requires the interactive selection of seed points on each bone [9]. Compared with these, our method of segmentation of femur and femoral neck based on region characteristics accurately detects both evenly- and unevenly-distributed bones. Our fully-automated segmentation technique with $DSC = 94.8\%$ is similar to the deep segmentation network with $DSC = 95.3\%$. However, the deep network required extensive training and large number of ground truth data [16]. Thus, the simplicity and flexibility of our automatic approach is of clinical use for hip joints with severely affected groups.

The limitation of this work is the small number of datasets. Future work should employ many databases using different scanners to improve the proposed method for segmentation and detection of fractures. The proposed framework focused on the segmentation of three different bone regions, and thus additional work to extract the quantitative morphometric features from different locations of the femur such as the head, neck, and trochanter would increase the value of the proposed framework for fracture identification.

VII. CONCLUSION

This study presented a complete automatic framework for the segmentation of both the left and right acetabulum, the femur,

and the femoral neck in hip joint CT images with severe abnormalities. The proposed methods for the segmentation of acetabulum based on bone height and joint space size is simple and performed robustly for unevenly-distributed bone structures. The experimental results based on 3D visualizations of the femoral neck showed that the proposed method is more accurate and improves subsequent measurements of bone fracture determination. Compared to the standard ACM and ASM, the segmentation performance of the femur by our proposed method produced high similarity agreement with the manual region segmentation method. However, the computational cost of manual segmentation is higher than our automatic method. Thus, the proposed framework could be both helpful and efficient in clinical use for severely affected hip joints with a risk of osteoporotic fracture.

REFERENCES

[1] V. Bousson, A. Le Le Bras, F. Roqueplan, Y. Kang, D. Mitton, S. Kolta, C. Bergot, W. Skalli, E. Vicaut, W. Kalender, K. Engelke, and J.-D. Laredo, "Volumetric quantitative computed tomography of the proximal femur: Relationships linking geometric and densitometric variables to bone strength. Role for compact bone," *Osteoporosis Int.*, vol. 17, no. 6, pp. 855–864, Mar. 2006.

[2] F. Johannesdottir, K. E. S. Poole, J. Reeve, K. Siggeirsdottir, T. Aspelund, B. Mogensen, B. Y. Jonsson, S. Sigurdsson, T. B. Harris, V. G. Gudnason, and G. Sigurdsson, "Distribution of cortical bone in the femoral neck and hip fracture: A prospective case-control analysis of 143 incident hip fractures; the AGES-REYKJAVIK study," *Bone*, vol. 48, no. 6, pp. 1268–1276, Jun. 2011.

[3] J. Panula, H. Pihlajamäki, V. M. Mattila, P. Jaatinen, T. Vahlberg, P. Aarnio, and S.-L. Kivelä, "Mortality and cause of death in hip fracture patients aged 65 or older—A population-based study," *BMC Musculoskeletal Disorders*, vol. 12, no. 1, pp. 1–6, May 2011.

[4] M. H. Moghari and P. Abolmaesumi, "Global registration of multiple bone fragments using statistical atlas models: Feasibility experiments," in *Proc. 30th Annu. Int. Conf. IEEE Eng. Med. Biol. Soc.*, Vancouver, BC, Canada, Aug. 2008, pp. 5374–5377.

[5] J. Wu, P. Davuluri, K. R. Ward, C. Cockrell, R. Hobson, and K. Najarian, "Fracture detection in traumatic pelvic CT images," *Int. J. Biomed. Imag.*, vol. 2012, pp. 1–10, Jan. 2012.

[6] S. Winkelbach, R. Westphal, and T. Goesling, "Pose estimation of cylindrical fragments for semi-automatic bone fracture reduction," in *Proc. DAGM-Symp.*, Magdeburg, Germany, 2003, pp. 566–573.

[7] Y. Kang, K. Engelke, and W. A. Kalender, "A new accurate and precise 3-D segmentation method for skeletal structures in volumetric CT data," *IEEE Trans. Med. Imag.*, vol. 22, no. 5, pp. 586–598, May 2003.

[8] M. S. Kavitha, S. Y. Park, M. S. Heo, and S. I. Chien, "Distributional variations in the quantitative cortical and trabecular bone radiographic measurements of mandible, between male and female populations of Korea, and its utilization," *PLoS ONE*, vol. 11, no. 12, pp. 1–13, Dec. 2016.

[9] R. A. Zoroofi, Y. Sato, T. Sasama, T. Nishii, N. Sugano, K. Yonenobu, H. Yoshikawa, T. Ochi, and S. Tamura, "Automated segmentation of acetabulum and femoral head from 3-D CT images," *IEEE Trans. Inf. Technol. Biomed.*, vol. 7, no. 4, pp. 329–343, Dec. 2003.

[10] D. D. Ruikar, K. C. Santosh, and R. S. Hegadi, "Automated fractured bone segmentation and labeling from CT images," *J. Med. Syst.*, vol. 43, no. 3, pp. 1–13, Feb. 2019.

[11] G. M. Campbell and A. Sophocleous, "Quantitative analysis of bone and soft tissue by micro-computed tomography: Applications to *ex vivo* and *in vivo* studies," *BoneKEy Rep.*, vol. 3, pp. 1–12, Aug. 2014.

[12] J. Calder, A. M. Tahmasebi, and A.-R. Mansouri, "A variational approach to bone segmentation in CT images," in *Proc. Med. Imag., Image Process.*, Orlando, FL, USA, Mar. 2011, pp. 1–15.

[13] J. Wu, A. Belle, R. H. Hargraves, C. Cockrell, Y. Tang, and K. Najarian, "Bone segmentation and 3D visualization of CT images for traumatic pelvic injuries," *Int. J. Imag. Syst. Technol.*, vol. 24, no. 1, pp. 29–38, Feb. 2014.

[14] R. Bryan, P. B. Nair, and M. Taylor, "Use of a statistical model of the whole femur in a large scale, multi-model study of femoral neck fracture risk," *J. Biomech.*, vol. 42, no. 13, pp. 2171–2176, Sep. 2009.

[15] V. Sapthagirivasan, M. Anburajan, and S. Janarthanam, "Extraction of 3D femur neck trabecular bone architecture from clinical CT images in osteoporotic evaluation: A novel framework," *J. Med. Syst.*, vol. 39, no. 8, p. 81, Jul. 2015.

[16] S. Ghose, P. B. Greer, J. Sun, P. Pichler, D. Rivest-Henault, J. Mitra, H. Richardson, C. Wratten, J. Martin, J. Arm, L. Best, and J. A. Dowling, "Regression and statistical shape model based substitute CT generation for MRI alone external beam radiation therapy from standard clinical MRI sequences," *Phys. Med. Biol.*, vol. 62, no. 22, pp. 8566–8580, Oct. 2017.

[17] E. A. Audenaert, J. Van Houcke, D. F. Almeida, L. Paelinck, M. Peiffer, G. Steenackers, and D. Vandermeulen, "Cascaded statistical shape model based segmentation of the full lower limb in CT," *Comput. Methods Biomech. Biomed. Eng.*, vol. 22, no. 6, pp. 644–657, Mar. 2019.

[18] B. Besler, A. S. Michalaski, N. D. Forkert, and S. K. Boyd, "Automatic full femur segmentation from computed tomography datasets using an atlas-based approach," in *Proc. Compt. Methods Clin. Appl. Musculoskelet Imag.*, Quebec, QC, Canada, 2017, pp. 120–132.

[19] C. Chu, J. Bai, X. Wu, and G. Zheng, "MASCG: Multi-atlas segmentation constrained graph method for accurate segmentation of hip CT images," *Med. Image Anal.*, vol. 26, no. 1, pp. 173–184, Dec. 2015.

[20] N. Sarkalkan, H. Weinans, and A. A. Zadpoor, "Statistical shape and appearance models of bones," *Bone*, vol. 60, pp. 129–140, Mar. 2014.

[21] T. Heimann and H.-P. Meinzer, "Statistical shape models for 3D medical image segmentation: A review," *Med. Image Anal.*, vol. 13, no. 4, pp. 543–563, Aug. 2009.

[22] C. M. Deniz, S. Xiang, R. S. Hallyburton, A. Welbeck, J. S. Babb, S. Honig, K. Cho, and G. Chang, "Segmentation of the proximal femur from MR images using deep convolutional neural networks," *Sci. Rep.*, vol. 8, no. 1, pp. 1–14, Nov. 2018.

[23] F. Chen, J. Liu, Z. Zhao, M. Zhu, and H. Liao, "Three-dimensional feature-enhanced network for automatic femur segmentation," *IEEE J. Biomed. Health Informat.*, vol. 23, no. 1, pp. 243–252, Jan. 2019.

[24] S. J. Lim and Y. S. Park, "Plain radiography of the hip: A review of radiographic techniques and image features," *Hip Pelvis*, vol. 27, no. 3, pp. 125–134, Sep. 2015.

[25] T. Sözen, L. Özişik, and N. Ç. Başaran, "An overview and management of osteoporosis," *Eur. J. Rheumatol.*, vol. 4, no. 1, pp. 46–56, Mar. 2017.

[26] M. S. Kavitha, A. Asano, A. Taguchi, T. Kurita, and M. Sanada, "Diagnosis of osteoporosis from dental panoramic radiographs using the support vector machine method in a computer-aided system," *BMC Med. Imag.*, vol. 12, no. 1, pp. 1–11, Jan. 2012.

[27] M. S. Kavitha, F. Samopa, A. Asano, A. Taguchi, and M. Sanada, "Computer-aided measurement of mandibular cortical width on dental panoramic radiographs for identifying osteoporosis," *J. Investigative Clin. Dentistry*, vol. 3, no. 1, pp. 36–44, Feb. 2012.

[28] L. He, X. Ren, Q. Gao, X. Zhao, B. Yao, and Y. Chao, "The connected-component labeling problem: A review of state-of-the-art algorithms," *Pattern Recognit.*, vol. 70, pp. 25–43, Oct. 2017.

[29] N. Otsu, "A threshold selection method from gray-level histograms," *IEEE Trans. Syst., Man, Cybern.*, vol. 9, no. 1, pp. 62–66, Jan. 1979.

[30] O. Demirkaya, M. H. Asyali, and P. K. Sahoo, "Intensity-based image segmentation," in *Image Processing With MATLAB: Applications in Medicine and Biology*, 1st ed. Boca Raton, FL, USA: CRC Press, 2008, pp. 223–269.

[31] J. Canny, "A computational approach to edge detection," *IEEE Trans. Pattern Anal. Mach. Intell.*, vol. PAMI-8, no. 6, pp. 679–698, Nov. 1986.

[32] R. Jain, R. Kasturi, and B. G. Schunck, "Contours," in *Machine Vision*, 1st ed. New York, NY, USA: McGraw-Hill, 1995, pp. 218–223.

[33] A. Sarti, R. Malladi, and J. A. Sethian, "Subjective surfaces: A method for completing missing boundaries," *Proc. Nat. Acad. Sci. USA*, vol. 97, no. 12, pp. 6258–6263, Jun. 2000.

[34] V. Caselles, R. Kimmel, and G. Sapiro, "Geodesic active contours," *Int. J. Comput. Vis.*, vol. 22, no. 1, pp. 61–79, Feb. 1997.

[35] M. Kass, A. Witkin, and D. Terzopoulos, "Snakes: Active contour models," *Int. J. Comput. Vis.*, vol. 1, no. 4, pp. 321–331, Jan. 1988.

[36] B. van Ginneken, A. F. Frangi, J. J. Staal, B. M. Ter Haar Romeny, and M. A. Viergever, "Active shape model segmentation with optimal features," *IEEE Trans. Med. Imag.*, vol. 21, no. 8, pp. 924–933, Aug. 2002.

[37] T.-T. Wong and N.-Y. Yang, "Dependency analysis of accuracy estimates in k-fold cross validation," *IEEE Trans. Knowl. Data Eng.*, vol. 29, no. 11, pp. 2417–2427, Nov. 2017.

YOUNG-JI YUN (Graduate Student Member, IEEE) received the B.S. degree from the Department of Electronics Engineering, Kyungil University, Kyungsan, South Korea, in 2013, and the M.S. degree from the School of Electronics Engineering, Kyungpook National University, Daegu, South Korea, in 2015, where she is currently pursuing the Ph.D. degree. Her research interests include image processing and computer vision.

BYEONG-CHEOL AHN received the M.D. and Ph.D. degrees. He has been performing diagnostic nuclear medicine, theranostics practice for thyroid cancer patients and also basic research for the arena, including developing for redifferentiating agents for radioiodine refractory thyroid cancer using molecular imaging techniques as a nuclear medicine and internal medicine physician. He is also interested in cell-based therapy for thyroid cancer and in developing the therapy by applying molecular imaging techniques and in processing of medical imaging.

MUTHU SUBASH KAVITHA received the Ph.D. degree in information engineering from Hiroshima University, Japan, in 2012. Since 2012, she has been working as a Postdoctoral Fellow with Seoul National University. She was a Professor with Kyungpook National University, South Korea, until 2018. She is currently working as a JSPS Research Fellow with the Graduate School of Advanced Science and Engineering, Hiroshima University. Her research interests include image processing algorithms for image pattern analysis, machine learning, artificial intelligence, pattern recognition, and deep learning techniques.

SUNG-IL CHIEN (Member, IEEE) received the B.S. degree from Seoul National University, Seoul, South Korea, in 1977, the M.S. degree from the Korea Advanced Institute of Science and Technology, Daejeon, South Korea, in 1981, and the Ph.D. degree in electrical and computer engineering from Carnegie Mellon University, Pittsburgh, PA, USA, in 1988. Since 1981, he has been with the School of Electrical and Computer Engineering, Kyungpook National University, Daegu, South Korea, where he is currently a Professor. His research interests include computer vision, pattern recognition, and color image processing.